MEMS-Silicon Chip Bonding Verification using GHz Pulse-echo Simulation and Measurements

Shyam Trivedi*, Yi Xuan Yeo*, Mantalena Sarafianou*, Eva Leong Ching Wai*, Jaibir Sharma*, Daniel Ssu-Han Chen*, Amit Lal†, Kevin Tshun Chuan Chai*
*Institute of Microeletronics, Agency for Science, Technology and Research (A*STAR), Singapore
†SonicMEMS Laboratory, School of Electrical and Computer Engineering, Cornell University, Ithaca, NY, USA
trivedi_shyam@ime.a-star.edu.sg

***Abstract*—This research presents a novel method to differentiate the bonding quality of a MEMS chip to a silicon substrate by using bulk acoustic wave (BAW) transducer arrays to determine the GHz ultrasonic wave transmission through the bonding interface. Prior to bonding, one-port S-parameter measurements were conducted on the array device at the wafer level to determine the mean resonance frequency (1.487 GHz) and standard deviation (33.8 MHz). The MEMS chip was then bonded to a silicon substrate using Au-AuSn bonding at a temperature <300°C, and confocal scanning acoustic microscopy (CSAM) was used to verify the bond uniformity. The bonding completion was evaluated by exciting the MEMS transducers with an RF signal of 80 ns width centered at 1.47 GHz to generate a packet of bulk acoustic waves and assess the reflected echo signals. Finite element (FE) time-domain simulations were carried out for the 2D-array to analyze the pattern and peak-to-peak amplitudes of the first four echoes, as visual inspection alone was insufficient to confirm bonding. The simulation results revealed a unique signature that indicated bonding completion: the third-echo amplitude became larger than the second-echo when the bonding percentage was >70%, due to constructive interference of ultrasonic waves reflected from the bonding interface and the substrate bottom. For fully bonded cases, the fourth echo became larger or comparable to the second echo, and first echo levels diminish by at least 20%. Electro-acoustic measurements were performed before and after bonding to confirm these distinctive signatures and categorize the devices as fully bonded, partially bonded, or unbonded.**

***Index Terms*—Acoustic Transmission, AlN Piezoelectric, BAW Transducers, GHz, Gold-Tin Bonding, Pulse-echo, Ultrasonic, Wavefront**

I. Introduction

Fourier transform (FT) is extensively used for signal processing, computation, and data analysis in various fields of engineering. In comparison to the standard discrete Fourier transform (DFT), the 2D Fast Fourier transform (FFT) can efficiently complete $O(N^2 \log N)$ arithmetic operations for N×N inputs [1]. Further improvement in computational speeds can be achieved by utilizing optical or ultrasonic FFT techniques that exploit the principle that spatial distribution of wave intensity at the receiver plane is representative of the Fourier transform of the transmitting wavefront [2]. Controlling the magnitude and phase of the input wave is challenging in optical FFT. However, ultrasonic wavefront computing (WFC) provides an efficient, miniaturized, and compact alternative to control the amplitude and phase of the ultrasonic wave by driving a piezoelectric phased array with GHz signals [3], [4].

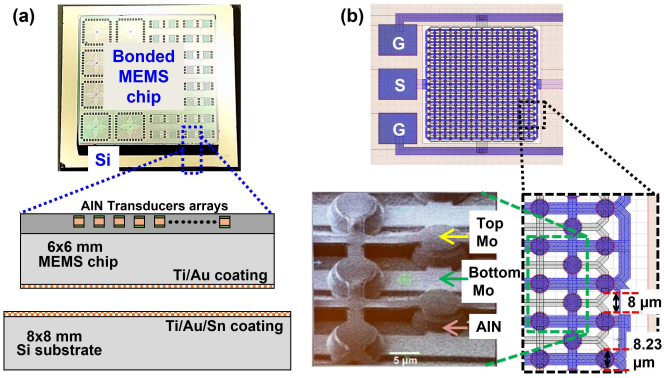

Fig. 1. (a) MEMS chip bonded to silicon substrate via the Au-AuSn bonding interface. The MEMS chip (6×6 mm) with AlN transducers are bonded to silicon substrate (8×8 mm) (b) Layout of the BAW array with zoom-in portion showing the diameter (8.23 µm) and spacing (8 µm) of elements in a closed-pack arrangement. AlN is sandwiched between Mo electrodes.

The fabrication of an ultrasonic WFC system poses various engineering challenges, including the development of CMOS-MEMS transducers, Fresnel lenses [5], and the proper bonding of these chips to the silicon substrate at temperatures lower than <300°C to enable efficient transmission and reception of GHz acoustic waves [6]. A uniform and thin bonding interface with minimal voids is necessary to minimize acoustic wave attenuation and mode conversion. While confocal scanning acoustic microscopy (CSAM) and optical images can provide visual clues, they are often insufficient to confirm successful bonding. In this study, we present a novel pulse-echo time domain approach that uses echo amplitudes to verify the bonding of the MEMS chip to the silicon substrate through measurements and simulations.

II. Device Description

MEMS chip bonded to silicon substrate is shown in Fig. 1(a). The right-half of the chip consists of 32 bulk acoustic wave (BAW) array devices. The back side is deposited with Au layer with Ti acting as an adhesion promoter. The bottom silicon substrate is coated with Ti followed by Au and Sn. The Au and Au/Sn layers of the two surfaces are fused together at

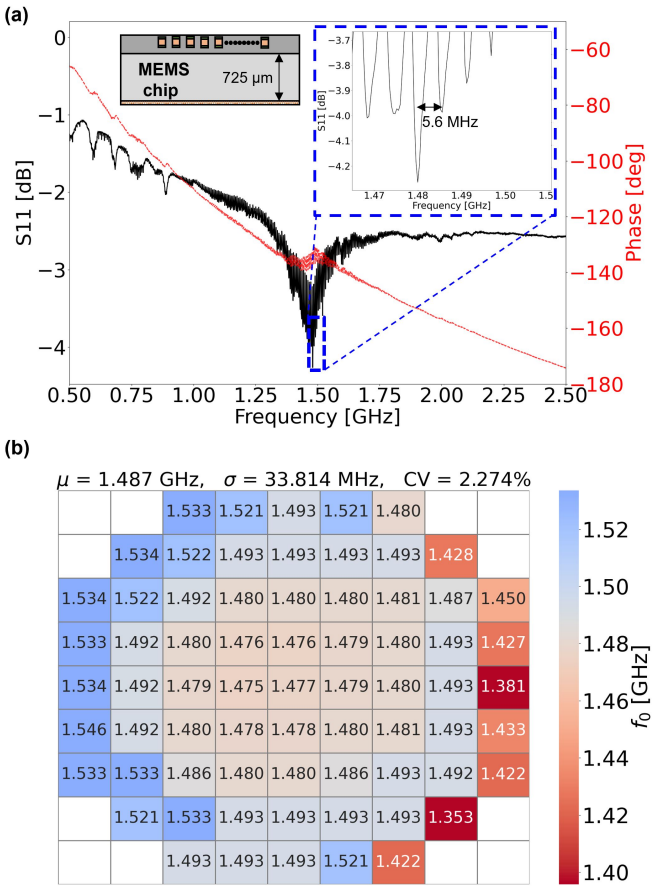

Fig. 2. (a) One port S_{11} measurement showing the magnitude (dB) and phase (deg) variation with frequency of the BAW array. Inset shows the zoom-in around the resonance with cavity mode separation of 5.6 MHz. (b) Wafer-level heat-map showing the variation in resonance frequency with position. The mean value of resonance, standard deviation and coefficient of variation are 1.478 GHz, 33.8 MHz, and 2.27% respectively.

temperatures ranging from 280-300°C via eutectic bonding. The bonding interface is ~500 nm thick, with the Au/Sn bonding interface containing 80% Au by weight. The bonding process is carried out manually using a customized chip bonder that places the MEMS chip and the silicon substrate between two larger ceramic plates by applying a force of ~50 N. The pressed sample is then taken out and placed in an oven with N_2 ambient environment to ensure uniform bonding between two surfaces [7]. The bonded sample is later used for pulse-echo measurements.

Fig. 1(b) shows the detailed layout of the array design with ground-signal-ground (GSG) pads. The AlN transducer array is composed of 389 circular high-overtone bulk acoustic wave resonator (HBAR) elements. The array is comprised of 389 devices arranged in a closed-pack structure with a total of 21 columns. The array distribution consists of 11 columns with 19 devices and 10 columns with 18 devices each. The diameter of each element is 8.32 µm with a spacing of 8 µm. The AlN layer is sandwiched between the top and bottom Mo electrodes and the entire array is encapsulated with SiO_2.

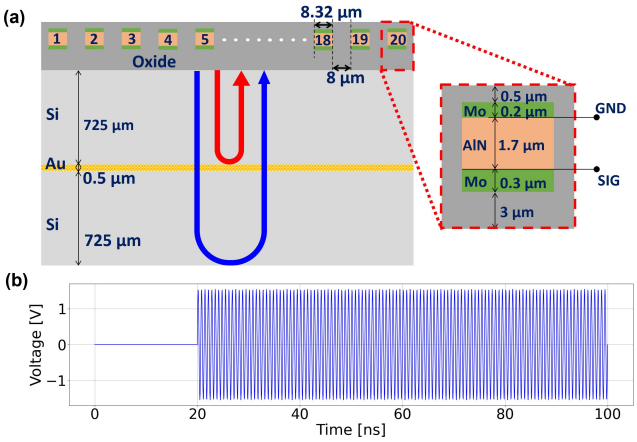

Fig. 3. (a) Simulation geometry showing the 2D piezoelectric array with 725 µm silicon substrate, 500 nm Au bonding interface and 1.7 µm AlN piezoelectric layer (b) Excitation signal of 1.48 GHz with 80 ns active period applied to the array.

III. S-Parameter Measurements

Prior to bonding, one of the array positioned in the middle of the die was chosen and one port S_{11} measurement was carried out on wafer-level to study the trend ofdevice resonance across the entire wafer. Fig. 2(a) shows the variation in dB and phase response of the BAW array with a weak resonance centered at ~1.47 GHz. The cavity modes of the array gets suppressed above and below this resonance. The zoom-in inset image around the resonance shows that the cavity modes of the HBAR array are separated by 5.6 MHz which corresponds to a transit time of ~178 ns in 725 µm long silicon MEMS chip. Similar transit time is obtained for subsequent echoes in both pulse-echo measurements and time-domain 2D simulations of the array. Fig. 2(b) shows the wafer-level heat map highlighting the positional variation of the resonance frequency with a mean value of 1.487 GHz, standard deviation σ = 33.8 MHz, and coefficient of variation CV = 2.3%. The BAW array positioned to the left of the wafer displays higher resonance possibly because of increased stiffness while the devices towards the right show lower frequencies due to AlN thickness variations.

IV. Simulation Setup and Results

Time-domain finite element (FE) simulation of the 2D BAW array is performed using the piezoelectric MEMS module of COMSOL Multiphysics™ to study the transmission/reception (TX/RX) response of the bonded and unbonded cases. Since a full 3D simulation in the time domain is extremely difficult to perform considering the memory and time required to solve, a 2D array is made with dimensions illustrated in Fig. 3(a). Further reduction in meshing requirements was made by using the symmetry boundary condition and designing just half of the desired geometry. AlN film of 1.7 µm is present between the top and bottom Mo electrodes acting as ground and signal terminals respectively. An input signal of 100 ns duration with 80 ns active time is applied to the bottom electrode shown in

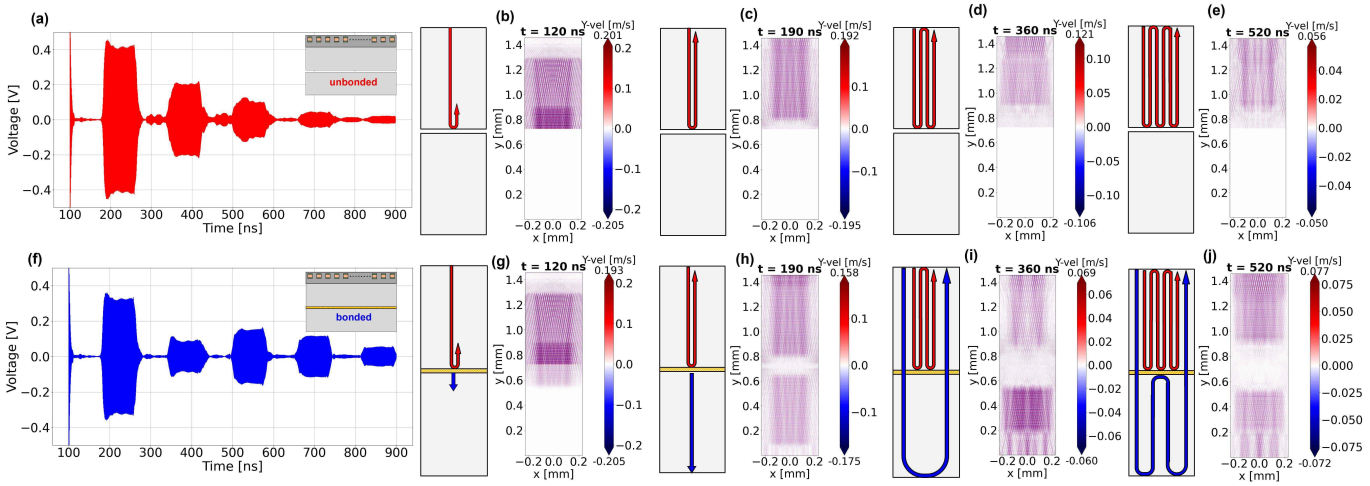

Fig. 4. (a) Voltage signal received for the unbonded scenario displays echoes that progressively decrease in amplitude. Wave propagation and surface plots of the Y-component of wave velocity are presented for time instants (b) 120 ns, (c) 190 ns, (d) 360 ns, and (e) 520 ns respectively for the unbonded case. (f) Voltage waveform received for the bonded cases displays a unique signature. Wave propagation and surface plots of the Y-component of wave velocity are presented for time instants (g) 120 ns, (h) 190 ns, (i) 360 ns, and (j) 520 ns respectively for the bonded case.

Fig. 3(b). The simulation is run from 0-900 ns with a time step of 50 ps. The signal terminal acts as a transmitter for the first 100 ns and as a receiver thereafter. The wavelength of the transmitted wave depends on frequency (1.48 GHz) and propagation velocity in silicon (8500 m/s) as $\lambda = v_{si}/f \sim$ 5.8 µm. The top and bottom silicon substrate need to mesh such that the maximum element size equates to at least $\lambda/10$ for successful spatial resolution of the wave. The simulation model generates nearly 400,000 elements and solves for 1.5M degrees of freedom. No damping loss is considered in the simulation since silicon is a low-loss material and the majority of the loss in propagation is due to the spreading of the wavefront. The left and right boundaries of the geometry are made as low-reflecting to avoid unwanted reflections affecting the main wavefront.

The RX waveform displays progressively decreasing echoes with time as shown in Fig. 4(a) for the unbonded case. The wave reaches the bonding interface in about 85 ns, gets reflected, and reaches the transducers back in ~170 ns. The wave velocity propagation at different instants is illustrated in Fig. 4(b-e) shows multiple reflections of the wave in the upper block as no energy penetrates the bottom substrate.

A bonded array device shows a significantly different signature of the RX waveform in comparison to the unbonded one (Fig. 4(f)) such that the peak-to-peak amplitude of the third echo becomes larger than the second echo. As shown in Fig. 4(g), at t~120 ns, the incident elastic wave after striking the interface gets reflected because of different acoustic impedance values of two materials at interface (Z_{Si} = 19.7 MRayl and Z_{Au} = 63.8 MRayl) layers. The reflection coefficient at interface $\Gamma = (Z_{Si} - Z_{Au})/(Z_{Si} - Z_{Au})$ indicates 53% of wave energy is reflected and the rest is transmitted in the bottom substrate. At t = 190 ns (Fig. 4(h)), the first echo is already received and the wave in the lower substrate hits the bottom boundary. At t = 360 ns (Fig. 4(i)), second echo with a smaller amplitude is received due to the interplay of two wave components. One of them encounters double reflection within the top substrate while the other one travels through to the bottom and transits back. The second echo reduces because of the destructive interference of these two wave components arriving together at the top surface. Alternatively, the third echo's amplitude gets boosted because of constructive interference of the wave (Fig. 4(j)). The maximum Y-velocity shown in Fig. 4(i) and Fig. 4(j) for time instants 360 ns and 520 ns respectively, also indicates that the third echo is larger than the second echo.

In order to investigate the impact of partial bonding on the RX waveform pattern, time-domain simulations were performed by varying the bonding percentage from 0% to 100% in increments of 10%. The peak-to-peak value of the first four echoes was determined for each simulation to facilitate a comparison. The schematic and Y-velocity surface plots at 120 ns for varying bonding percentages are depicted in Fig. 5(a)-(f). The results demonstrate that as larger portion of the substrate is bonded, a corresponding increase in energy transmitted to the substrate is observed.

The variation in normalized peak-to-peak RX voltage for the first four echoes with bonding percentage is plotted in Fig. 5(g). Some clear distinguishing signatures can be noted as we move from unbonded to bonded case. Firstly, both the first and the second echo amplitudes decrease by approximately 20% and 50% respectively. Secondly, echo amplitudes of the third and the fourth echo increases. Thirdly, once the sample is *mostly bonded* (>70%) the third echo amplitude becomes larger than the second echo. Finally, it is noted that the for 100% bonded case the amplitudes of fourth and second echo become comparable.

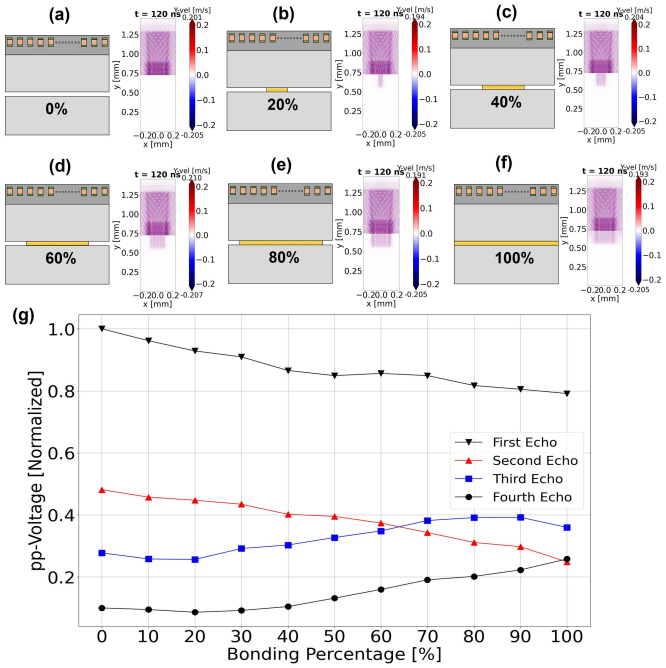

Fig. 5. Geometry showing the bonding percentage and Y-velocity surface plots at t = 120 ns for (a) 0%, (b) 20%, (c) 40%, (d) 60%, (e) 80%, and (d) 100% bonded cases. (g) Variation in normalized peak-to-peak RX voltage with bonding percentage for the first four echoes.

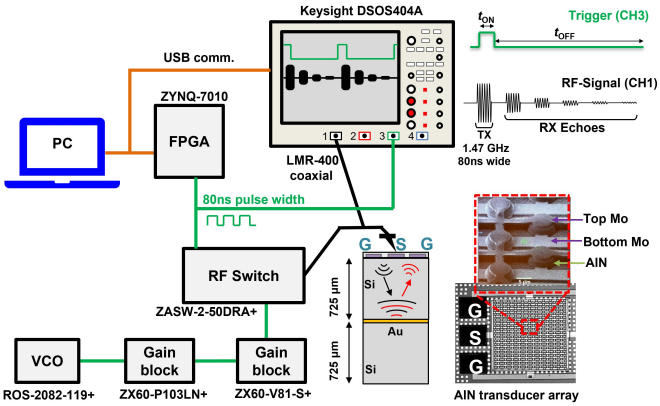

Fig. 6. The setup for electro-acoustic measurements for pulse-echo measurements involved a VCO, gain block, and RF switch to produce an 80 ns wide, 1.47 GHz excitation signal. The TX/RX signals were both captured in the same channel-1 via LMR-400 cable, while the trigger signal was displayed in channel 3 of the oscilloscope.

V. Measurement Setup, Results and Discussion

Fig. 6 depicts the setup for pulse-echo measurements on the MEMS chip bonded to silicon. The voltage-controlled oscillator (VCO) is adjusted to create an RF signal with a center frequency of 1.47 GHz. Two gain blocks with individual gains of 20 dBm and 21 dBm amplify the VCO signal. The Field Programmable Gate Array (FPGA) generates an 80 ns trigger signal, and the RF switch redirects the excitation signal to the GSG pads of the array for the same duration. The acoustic wave's transit time t_{tr} from the top of the silicon substrate to the bonding interface is t_{tr} = 725 µm/8500 m/s ~85 ns. The trigger signal duration is kept shorter than the transit time to prevent the reflected wave from interfering with the excitation wave. The trigger signal is detected by channel 3 of the oscilloscope, while channel 1 captures the applied TX signal and the RX echo signal from the same GSG probes. Electro-acoustic measurements were conducted before bonding to the silicon substrate and utilized as a reference for post-bonding measurements. The pulse-echo data of 32 array devices in the die were analyzed without any additional signal processing, and up to four echoes were visible before the signal was engulfed by background noise.

After the bonding process, CSAM image of the MEMS chip is taken as shown in Fig. 7(a). Upon inspection of the CSAM image, it appears to have a uniform appearance with darker areas indicating stronger bonding of MEMS chip with silicon substrate. The right half of the image displays an 8x4 grid containing 32 array devices. However, it is challenging to determine whether the devices are bonded or not solely based on visual inspection. Further analysis of the echo data reveals that bonding is not consistent across all devices, with some devices remaining unbonded or only partially bonded. Notably, devices located at the corners are subject to more stress and pressure during pressing with the substrate, resulting in a higher likelihood of successful bonding. In contrast, devices located in the middle of the grid may remain partially bonded or unbonded.

The measurement results of the array grid can be divided into three main categories, as shown in Fig. 7(b). A typical measurement response of a 100% bonded site is observed, where successful bonding results in a reduction of 20-25% in the peak-to-peak magnitude of the first echo. In addition, the magnitude of the third echo is greater than that of the second, and the magnitude of the fourth echo is either larger or comparable to that of the second echo. This pattern is consistent with the corresponding FE simulation result shown in Fig. 7(e). However, it is noted that in the 2D array simulation, the RX voltage levels are observed to be one order higher than the actual 3D measured results, although the pattern remains similar. Furthermore, it should be noted that the time-domain simulation does not include any Rayleigh damping.

Fig. 7(c) and (f) depict the results of measurements and simulations (60% bonded) for the partially bonded case. While a decrease in the magnitude of the first echo is observed, the magnitude of the third echo remains lower than that of the second echo, indicating that the device is still less than 70% bonded. However, quantifying the degree of partial bonding by comparing the 2D array simulation and measurement results is challenging due to the numerous ways in which a particular sample can be partially bonded in three dimensions.

Fig. 7(d) displays the measurement outcome for the unbonded scenario, whereas Fig. 7(g) illustrates the RX signal in the simulation for the 10% bonded case. A very minor reduction in the first echo indicates that no energy transfer takes place in the bottom substrate and entire signal

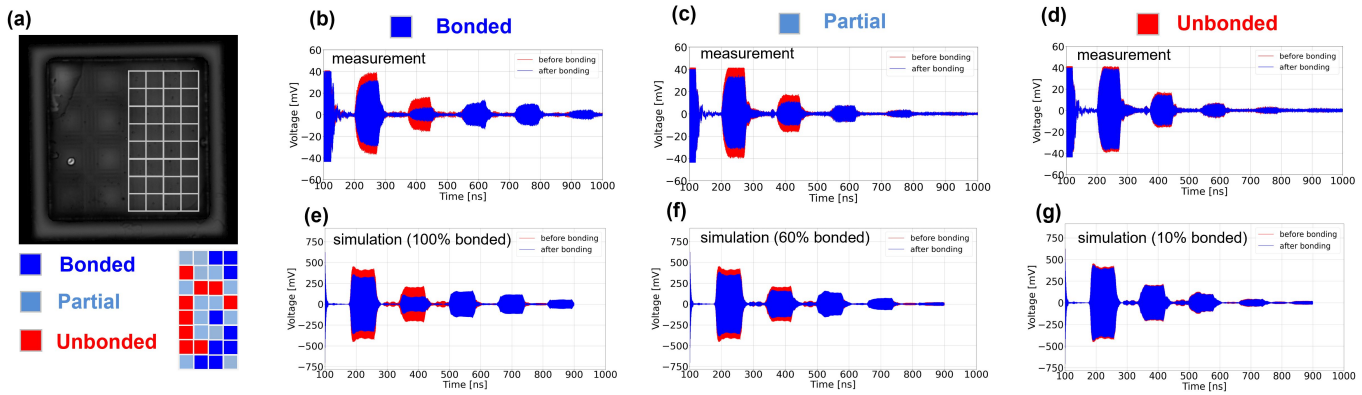

Fig. 7. (a) CSAM image of the MEMS die after bonding. The right-half of the chip shows the 8×4 grid with 32 array devices. From the measured pulse-echo response these can be broadly classified into three categories namely bonded, partial, and unbonded. Typical measured and simulation response before and after bonding are shown for (b), (e) successfully bonded sites with third echo magnitude larger than second, (c), (f) partially bonded case, and (d), (g) unbonded case with progressively decreasing echoes.

undergoes multiple reflections in the top silicon substrate with progressively decreasing echo amplitudes. The signal *after bonding* shows the same pattern as *before bonding* with very minor reduction in the overall amplitude.

VI. Conclusions and Future Work

This study has demonstrated the validation of the bonding process between a MEMS chip and a silicon wafer by analyzing the first four echo amplitudes, using a combination of pulse-echo measurements and time-domain 2D FE simulation. Prior to the bonding process, wafer-level one port S-parameter measurements were performed, confirming a mean resonance frequency of 1.487 GHz. The FE simulations indicated that the unbonded samples exhibit progressively decreasing echoes. In contrast, the bonded samples (>70%) display a distinct signature with a third echo amplitude larger than the second. The fully bonded samples exhibit fourth echo levels almost comparable to the second, while the first echo is reduced by 20% due to more energy being transmitted to the bottom substrate. Similar echo signatures were observed in the pulse-echo measurement results, and the samples were classified as bonded, unbonded, or partially bonded. The CSAM and optical images alone were insufficient to confirm bonding completion for different devices and pulse-echo measurements with FE simulations were shown to play a crucial role in the verification of bonding. For future research, a comprehensive statistical analysis can be conducted on a large dataset using the pulse-echo technique to quantify partial bonding. The impact of temperature on the bonding interface can be investigated. Additionally, comparing the wafer-level bonding process with the manual chip-level bonding process can also be explored.

Acknowledgment

This research was supported by A*STAR under the "Ultrasonic Wavefront Computing" grant (Grant No. A19E8b0102).

References

[1] Y. Liu, J. Kuo, M. Abdelmejeed, and A. Lal, "Optical measurement of ultrasonic fourier transforms," in *2018 IEEE International Ultrasonics Symposium (IUS)*, 2018, pp. 1–9.

[2] D. A. Patel, V. P. Bui, K. T. C. Chai, A. Lal, and M. M. S. Aly, "Sonicfft: A system architecture for ultrasonic-based fft acceleration," in *2022 27th Asia and South Pacific Design Automation Conference (ASP-DAC)*. IEEE, 2022, pp. 345–351.

[3] K.-H. Teng, S. Raju, D. Zhu, J. L. K. Lim, D. S.-H. Chen, E. W. L. Ching, S. Jaibir, L. E.-Y. Joshua, E. J. Ng, and K. T. C. Chai, "An on-chip 2-d dft accelerator ultrasonic wavefront for convolutional neural networks," in *2021 IEEE USNC-URSI Radio Science Meeting (Joint with AP-S Symposium)*. IEEE, 2021, pp. 124–125.

[4] M. Abdelmejeed, J. C. Kuo, and A. Lal, "Ghz ultrasonic digital to analog converter for wavefront signal processing," in *2018 IEEE International Ultrasonics Symposium (IUS)*, 2018, pp. 1–9.

[5] J. Hwang, J. Kuo, and A. Lal, "Planar ghz ultrasonic lens for fourier ultrasonics," in *2019 IEEE International Ultrasonics Symposium (IUS)*. IEEE, 2019, pp. 1735–1738.

[6] D. S. Chen, E. L. Wai, Y. X. Yeo, J. Sharma, A. Lal, and K. T. Chai, "Investigation of au-ausn bonding below eutectic temperature for gigahertz bulk acoustic wave transmission," in *2022 IEEE 24th Electronics Packaging Technology Conference (EPTC)*, 2022, pp. 315–320.

[7] D. S.-H. Chen, M. Sarafianou, E. L. C. Wai, J. Sharma, A. Lal, and K. T. C. Chai, "A study of bonding materials for ghz ultrasonic wavefront computing," in *2022 IEEE International Ultrasonics Symposium (IUS)*, 2022, pp. 1–4.